



Diamond surface functionalization via visible light-driven C-H activation for nanoscale quantum sensing

Lila V. H. Rodgers^{a,1}, Suong T. Nguyen^{b,1}, James H. Cox^b, Kalliope Zervas^a, Zhiyang Yuan^a, Sorawis Sangtawesin^{c,d}, Alastair Stacey^{e,f}, Cherno Jaye^g, Conan Weiland^g, Anton Pershin^{h,i}, Adam Gali^{h,i,j}, Lars Thomsen^k, Simon A. Meynell^l, Lillian B. Hughes^m, Ania C. Bleszynski Jayich^l, Xin Gui^b, Robert I. Cava^b, Robert R. Knowles^{b,2}, and Nathalie P. de Leon^{a,2}

Edited by David Awschalom, The University of Chicago, Chicago, IL; received September 14, 2023; accepted January 8, 2024

Nitrogen-vacancy (NV) centers in diamond are a promising platform for nanoscale NMR sensing. Despite significant progress toward using NV centers to detect and localize nuclear spins down to the single spin level, NV-based spectroscopy of individual, intact, arbitrary target molecules remains elusive. Such sensing requires that target molecules are immobilized within nanometers of NV centers with long spin coherence. The inert nature of diamond typically requires harsh functionalization techniques such as thermal annealing or plasma processing, limiting the scope of functional groups that can be attached to the surface. Solution-phase chemical methods can be readily generalized to install diverse functional groups, but they have not been widely explored for single-crystal diamond surfaces. Moreover, realizing shallow NV centers with long spin coherence times requires highly ordered single-crystal surfaces, and solution-phase functionalization has not yet been shown with such demanding conditions. In this work, we report a versatile strategy to directly functionalize C-H bonds on single-crystal diamond surfaces under ambient conditions using visible light, forming C-F, C-Cl, C-S, and C-N bonds at the surface. This method is compatible with NV centers within 10 nm of the surface with spin coherence times comparable to the state of the art. As a proof-of-principle demonstration, we use shallow ensembles of NV centers to detect nuclear spins from surface-bound functional groups. Our approach to surface functionalization opens the door to deploying NV centers as a tool for chemical sensing and single-molecule spectroscopy.

quantum sensing | photochemical C-H bond activation | surface functionalization | NV centers in diamond | surface spectroscopy

Nitrogen-vacancy (NV) centers in diamond are point defects in the diamond lattice that enable room temperature nanoscale NMR of small ensembles down to the interrogation of individual spins (1). In these experiments, an NV center is located within a few nanometers of a target molecule on the diamond surface, and the magnetic signal from spins in the target molecule perturbs the phase of the NV spin, which is detected optically (Fig. 1A). In recent years, NV centers have been used to detect magnetic noise arising from nuclear spins in a single ubiquitin protein (2) and from single electron spins at the diamond surface (3), perform NMR spectroscopy of microscale volumes of liquid with around 1 Hz spectral resolution (4), and spatially map individual ¹³C nuclear spins in the diamond lattice under cryogenic conditions (5). Despite this impressive progress, nanoscale NMR of arbitrary target molecules external to the diamond lattice remains elusive.

In order to sense a target molecule, the molecule must be immobilized within nanometers of an NV center with long spin coherence. Recent efforts to install such target molecules have used a thin layer (1 to 2 nm) of Al₂O₃ as a chemically functionalizable interface to attach sensing targets to diamond surfaces (6, 7). However, this approach comes at the expense of increased distance between NV sensor and target and has been shown to have some adverse effects on NV spin coherence. Directly functionalizing the diamond surface to attach sensing targets would eliminate the need for a separate material interface, but the chemical inertness (8) and small lattice constant of diamond make this approach challenging.

Conventional diamond surface functionalization methods for NV experiments operate under harsh conditions, relying on the use of plasma (9-11), thermal annealing (2, 12), or oxidizing acids (13). These approaches severely limit the scope of functional groups that can be attached and can damage the diamond surface, destabilizing shallow NV centers (12). Wet chemical methods allow for more controllable and mild surface modification methods, which enable covalent attachment of diverse functional groups to the surface. Thus far, wet chemical functionalization has been largely demonstrated on nanodiamonds (14), micro-crystalline diamonds (15, 16), or poly-crystalline diamonds

Significance

Quantum sensors based on nitrogen-vacancy (NV) centers in diamond can potentially be used for highly sensitive magnetic resonance measurements with nanoscale resolution. Developing such a platform requires immobilizing target molecules within a few nanometers of NV centers with long coherence times. An attractive strategy is to directly attach target molecules to the diamond surface; however, the inert nature of diamond typically necessitates harsh or defect-mediated chemistry, limiting the scope of surface functionalization. This work establishes a methodology and approach for functionalizing low-defect, single-crystal diamond surfaces using gentle, wet chemical techniques that are compatible with coherent NV centers within nanometers of the surface, opening the door to deploying NV centers as a broad tool for chemical sensing and single-molecule spectroscopy.

Competing interest statement: L.V.H.R., S.T.N., R.R.K., and N.P.d.L. have filed for a patent that relates to this work. The authors declare no other competing interests.

This article is a PNAS Direct Submission.

Copyright © 2024 the Author(s). Published by PNAS. This article is distributed under Creative Commons Attribution-NonCommercial-NoDerivatives License 4.0 (CC BY-NC-ND).

¹L.V.H.R. and S.T.N. contributed equally to this work.

²To whom correspondence may be addressed. Email: rknowles@princeton.edu or npdeleon@princeton.edu.

This article contains supporting information online at https://www.pnas.org/lookup/suppl/doi:10.1073/pnas. 2316032121/-/DCSupplemental.

Published March 7, 2024.

(17-19), but these materials have a wide range of crystal faces and their surface chemistry is dominated by grain boundaries and high concentrations of defects such as sp²-bonded and amorphous carbon (20). Additionally, the spin coherence of shallow NV centers can vary by over an order of magnitude because of the presence of electronic defects at the surface arising from subtle differences in surface disorder (12). This makes it challenging to translate these techniques to high-purity, single-crystal diamonds required for NV-based nanoscale NMR sensing. Prior solution-phase functionalization chemistries have not been demonstrated on pristine surfaces with coherent, shallow NV centers. Recent work has demonstrated that plasma termination followed by subsequent functionalization of amide groups can be compatible with shallow NV centers (11). Additionally, a prior work has shown that defect-mediated photoexcitation of free carriers in the diamond via sub-bandgap ultraviolet light can initiate alkylation of hydrogen-terminated (H-terminated) single crystal diamond surfaces (21, 22) and allows for grafting molecules with exceptional biochemical functionality, demonstrated by the specific biomolecular binding properties of DNA-modified surfaces and the chemical stability of functional groups (23). This motivates a broader search for single-crystal surface functionalization methods and a study of their compatibility with shallow NV centers.

In this study, we present a generalizable photochemical strategy to functionalize high-quality, single-crystalline diamond surfaces, enabling the direct covalent attachment of diverse functional motifs, and we demonstrate the compatibility of this chemistry with shallow NV centers with long spin coherence. Inspired by recent developments in visible-light photocatalysis for activating C–H bonds in small molecules (24, 25), we set out to activate inert chemical bonds on diamond surfaces using photoactivated hydrogen atom transfer (HAT) reagents (Fig. 1B). These HAT reagents

homolyze C-H bonds on a hydrogen-terminated (H-terminated) diamond surface to generate carbon-centered radicals, which can be intercepted with various radical acceptors to form new carbonheteroatom bonds on the surface (Fig. 1 C). These solution-phase photochemical reactions operate at room temperature and enable the formation of various chemical bonds with surface coverages up to 10% (1.6 molecules/nm²), including C-F, C-Cl, C-S, and C-N bonds. We establish evidence for covalent bond formation on single-crystal surfaces using multimodal surface spectroscopies and develop a mechanistic understanding of the surface reactivity of single-crystal diamond. Finally, we show that functionalized surfaces are compatible with NV centers within 10 nm of the surface with spin coherence times comparable to the state of the art, and we use ensembles of shallow NV centers to detect nuclear spins (19F) contained in installed functional groups at the surface. This chemical strategy opens the door to a broad range of functionalization targets, thus overcoming a major hurdle for NV nanoscale molecular sensing.

We began by preparing high-quality, ultra-smooth, H-terminated diamond surfaces from oxygen-terminated surfaces (Fig. 1*C* and *Materials and Methods* and *SI Appendix* for more details) and establishing a general procedure to reliably evaluate the outcome of functionalization reactions. Briefly, the methodology for fabricating oxygen-terminated surfaces follows previous work (12) and includes polishing, etching, graphitizing, and annealing under an atmosphere of oxygen, or using the "as-grown" surface in the case of ¹²C isotopically purified material. After subjecting to hydrogen termination and a functionalization reaction, the samples were thoroughly cleaned in a mixture of solvents to remove physisorbed contaminants. To evaluate whether or not a reaction is successful, we cannot rely on traditional solution-phase chemical analysis tools because they do not have sufficient sensitivity to probe surfaces.

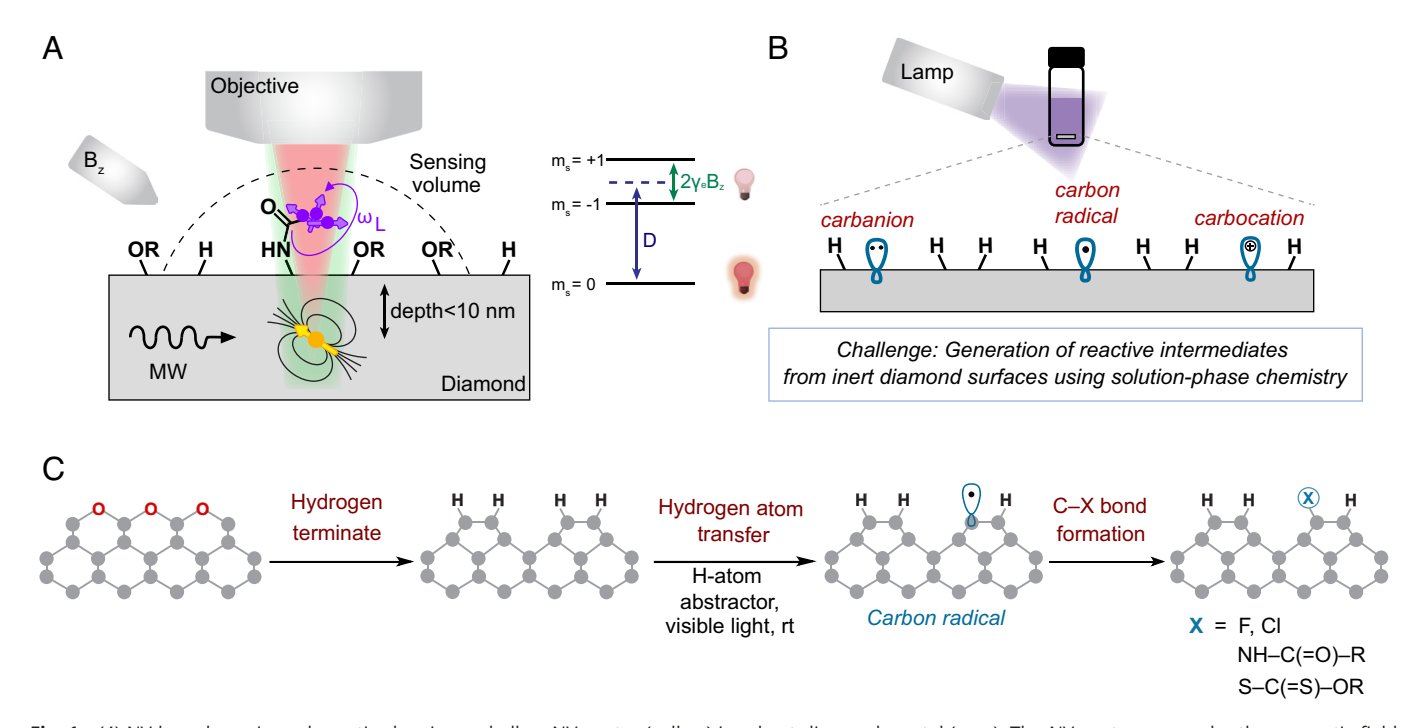


Fig. 1. (*A*) NV-based sensing schematic showing a shallow NV center (yellow) in a host diamond crystal (gray). The NV center can probe the magnetic field originating from functional groups containing nuclear spins (purple) that are covalently bonded to the surface and that precess at the Larmor frequency (ω) determined by their gyromagnetic ratio and the applied magnetic field (B_2). A green laser is used to optically initialize and read out the spin state of the NV center at room temperature and the spin-dependent red fluorescence is collected by a microscope objective. *Top Right*: NV ground-state energy level diagram with spin-dependent optical fluorescence showing zero field (D) and Zeeman splittings ($2γ_eB_2$). (*B*) The generation of reactive intermediates from inert surfaces using solution-phase chemistry is a long-standing challenge in diamond surface functionalization. (*C*) C–H bond activation via photochemical hydrogen atom transfer at room temperature (rt) enables the formation of a wide range of carbon-heteroatom bonds on diamond surfaces.

Thus, we sought to functionalize the surfaces with functional groups containing identifiable heteroatoms (e.g., N, S, halogens) and used surface-sensitive techniques such as X-ray photoelectron spectroscopy (XPS) to detect their presence on the surface. Since non-specific binding can also lead to spurious XPS signals (SI Appendix, Fig. S6), we iteratively cleaned our samples, checked for the consistency of the heteroatom signal in XPS, and verified that other contaminants from the reaction mixture were not present. Additionally, since physisorbed contamination and submonolayer deposition of polymerized material is unlikely to result in a well-ordered monolayer, we used atomic force microscopy (AFM) to check that the surface was smooth (SI Appendix, Fig. S9). XPS and AFM allow for rapid feedback for reaction discovery but do not provide conclusive evidence of covalent bond formation. To confirm our results, we performed more detailed spectroscopy using synchrotron near-edge X-ray absorption fine-structure spectroscopy (NEXAFS). A strong polarization dependence of the NEXAFS signal associated with the heteroatom of interest indicates that the attached functional group has a well-defined orientation relative to the diamond surface, providing compelling evidence of covalent bond formation (26).

As an example, we first developed an HAT method for fluorination of the H-terminated surface. This reaction involved the irradiation of the H-terminated diamond in acetonitrile solvent with tetrabutylammonium decatungstate (TBADT), a fluorinating reagent such as Selectfluor or N-fluorobenzenesulfonimide (NFSI), and sodium bicarbonate with 390-nm light at room temperature for 2 d (Fig. 2A). XPS analysis of the sample after the reaction and cleaning shows a clear F 1s signal (Fig. 2B and SI Appendix, Fig. S11) and verifies the absence of heteroatoms associated with other contaminants from the reaction mixture (SI Appendix, Fig. S7). Running the reaction in the dark did not result in an F 1s peak, indicating that light is required to achieve surface functionalization (Fig. $2\bar{C}$). Notably, the \hat{F} 1s peak did not diminish after multiple cycles of cleaning with organic solvents or after boiling in a mixture of concentrated sulfuric, nitric, and perchloric acids ("triacid cleaning") (Fig. 2B). AFM reveals that the surface morphology is smooth after the functionalization reaction and that it is free of precipitates (Fig. 2E). NEXAFS at the F K-edge shows a clear angular dependence, indicating that the C-F bonds are well-oriented on the surface (Fig. 2D and SI Appendix, Fig. S10). Low-energy electron diffraction (LEED) of a fluorinated surface shows a clear 2 × 1 pattern, which is consistent with an F/H mixed termination and demonstrates that the resulting surface is highly ordered (Fig. 2F). Quantitative analysis of XPS spectra reveals that the newly formed C-F bonds comprise (6 to 10)% surface coverage [(0.9 to 1.6) molecules/nm²], which is slightly lower than but comparable to the efficiencies of other mild processes for diamond surface functionalization (21, 27). We hypothesize that this moderate yield arises from a self-deactivation mechanism, in which the formation of C-F bonds increases the bond strength and electrophilicity of adjacent C-H bonds due to the strong electron-withdrawing effect of fluorine. Such deactivation effects are well documented in C-H fluorination studies with small molecule substrates (28, 29). We note that we also observe an increase in oxygen at the surface after functionalization and cleaning, indicating the possible presence of side reactions (SI Appendix, Fig. S31).

Using this HAT method and reaction discovery pipeline, we were also able to install other functional groups on the surface. Inspired by the work of Alexanian and co-workers (31), we found that treating the surface with N-chloroamide 1 in benzene under 456 nm light irradiation for 24 h resulted in chlorination of the surface with ≈4% coverage (0.6 molecules/nm²), which was confirmed by the appearance of a Cl 2p XPS signal (Fig. 2 G, Bottom Right, SI Appendix). Similarly, we installed xanthate groups with ≈2% coverage (0.3 molecules/nm²) by irradiating the sample in the presence of N-xanthylamide 2 for 24 h with 456 nm light, as evidenced by the appearance of an S 2p XPS signal (Fig. 2 G, Bottom Left) (32).

To further diversify the scope of structural motifs that can be attached to the surface, we sought to install a versatile functional handle that is amenable to a wide range of subsequent derivatization reactions. Serendipitously, we found that conducting the fluorination reaction with either Selectfluor or NFSI in the absence of the TBADT photocatalyst resulted in the formation of not only C-F bonds but also amide groups on the surface. This was evidenced by a clear N 1 s signal in XPS and an angle dependence at the N K-edge in NEXAFS (Fig. 3A and SI Appendix, Fig. S20). Though the identity of the nitrogen-containing group is not evident from the XPS or NEXAFS spectra, we were able to confirm the formation of amide groups by performing a series of control experiments with adamantane as a model substrate as well as with the diamond surface (See SI Appendix for more details). Furthermore, by replacing acetonitrile with 3,3,3-trifluoropropionitrile and trichloroacetonitrile, we also installed trifluoropropanamide and trichloroacetamide groups on the surface, respectively (Fig. 3B). These amide groups present opportunities to subsequently attach molecules of interest through amide coupling reactions, which are a standard strategy for attaching amino acids (33). Accordingly, amide-terminated surfaces were subjected to a hydrolysis reaction to form free amines. These amine groups are structurally similar to tert-butylamine and are thus expected to be considerably less reactive than typical primary amines due to their steric hindrance. Nevertheless, they still reacted with various acyl chlorides to install pentafluorobenzamide (Fig. 3C), 3,5-bis(trifluoromethyl)benzamide, and heptafluorobutyramide moieties on the surface (SI Appendix, Fig. S28). Though amide and amine are indistinguishable in XPS, we observed distinct X-ray absorption features at the N K-edge and O K-edge in NEXAFS, consistent with prior literature reports (34, 35) (SI Appendix,

Collectively, this diverse set of functionalization reactions not only enables the construction of various structural motifs on the surface but also allows us to understand the mechanisms behind these reactions on single-crystal diamond surfaces. Density functional theory (DFT) calculations estimate the bond dissociation energy (BDE) of C_{surface}-H to be ≈98 kcal/mol (SI Appendix, Fig. S34), which is similar to that of nonactivated tertiary C-H bonds in small molecules (e.g., C-H BDE in adamantane ≈99 kcal/mol) (37). In the fluorination reaction, surface C–H bonds could be abstracted by the excited state decatungstate anion $(W_{10}O_{32})^{4-}$, (38) the aminium radical cation (N–H BDFE ≈ 100 kcal/mol) (39) generated from Selectfluor, or the disulfonamidyl radical (N–H BDFE (≈105 to 110) kcal/mol) (40) produced from NFSI. The resulting carbon radicals could intercept either Selectfluor or NFSI to form new C-F bonds on the surface. Similarly, in the chlorination and xanthylation reactions, electrophilic amidyl radicals (N–H BDFE ≈ 110 kcal/mol) (41) generated from the light-driven homolysis of amides 1 and 2 could abstract surface C-H bonds to furnish the same carbon radical intermediates, which then react with 1 or 2 to install chlorine or xanthate groups, respectively (SI Appendix, Fig. S13) (31, 32). In the C-N bond formation reaction, the alkyl radicals undergo single electron transfer with Selectfluor (e.g., $E_{\rm red}$ (Selectfluor) \approx -0.04 V vs. SCE in MeCN (42), E_{ox} (tert-butyl radical) = 0.09 V vs. SCE in MeCN) (43). This process produces tertiary carbocations that can be trapped by a nitrile nucleophile to form C-N bonds via a Ritter mechanism (SI Appendix, Fig. S21) (39).

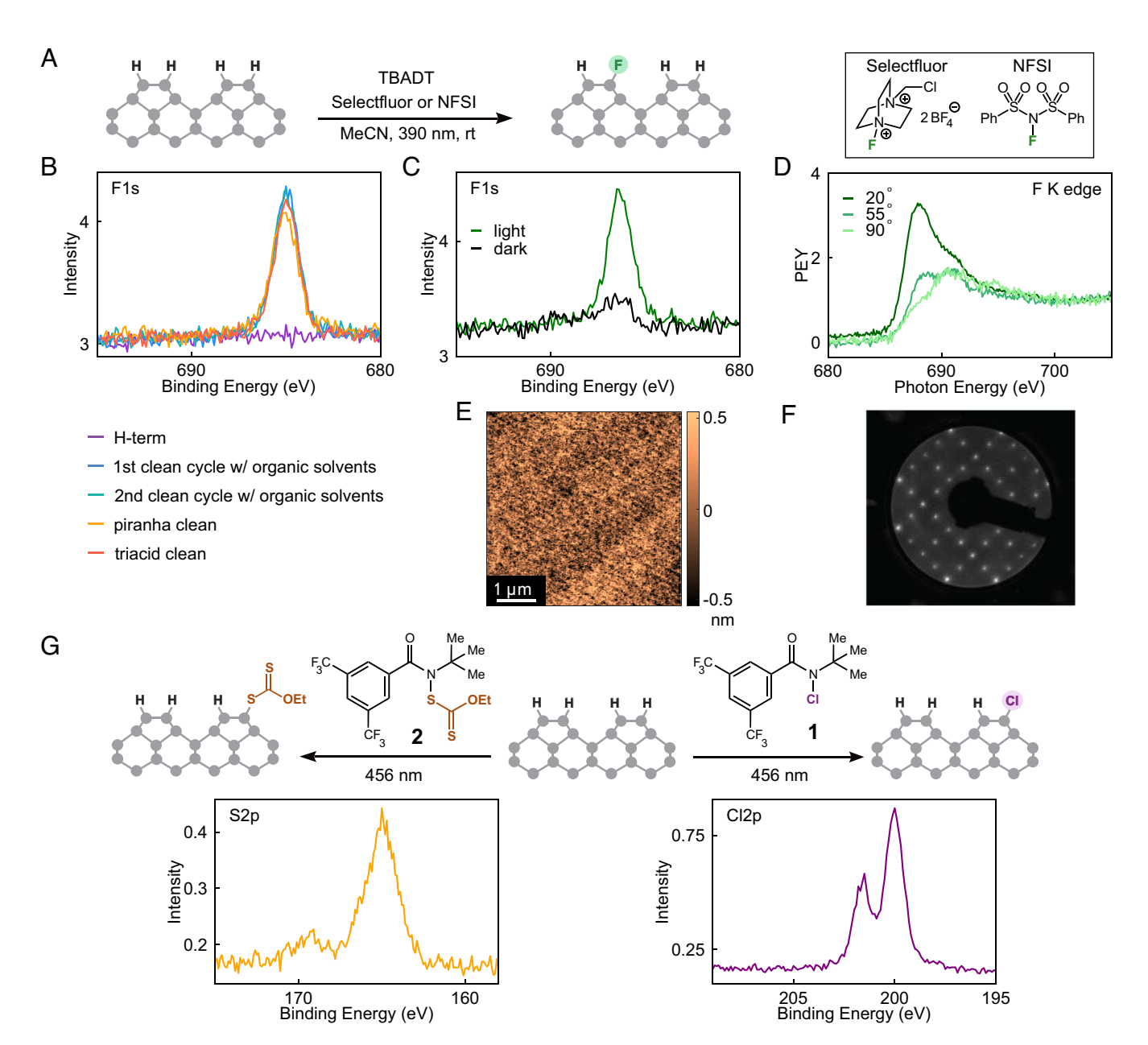


Fig. 2. Activation of C–H bonds via HAT enables fluorination, chlorination, and xanthylation reactions on diamond surfaces. (*A*) Reaction scheme for photochemical fluorination reaction (*Left*) with two fluorinating reagents: Selectfluor and NSFI (*Right*). (*B*) XPS F *1s* spectra of a fluorinated surface after iterative cleaning procedures. (*C*) F *1s* spectra for control experiments performed with and without light, showing that light is necessary to achieve fluorination. (*D*) NEXAFS F *K*-edge partial electron yield (PEY) spectra acquired at different angles of incidence. The observed angle dependence indicates the fluorine atoms are well-oriented on the surface, consistent with covalent bond formation. (*E*) AFM image of a functionalized diamond surface. The resulting surface is smooth ($R_a = 201 \text{ pm} \pm 6 \text{ pm}$), and there is no evidence of physisorbed contamination. Samples in (*B*–*D*) were fluorinated with NFSI, and samples in (*E*), and (*F*) were fluorinated with Selectfluor. XPS and NEXAFS spectra for samples fluorinated with Selectfluor are included in *SI Appendix*, Figs. S10 and S11. (*F*) LEED image of a fluorinated surface shows a 2 × 1 pattern, which is consistent with a mixed F/H termination and indicates that the surface is highly ordered. (*G*) *Top*: reaction schemes for xanthylation (*Left*) and chlorination (*Right*) reactions. *Bottom Left*: XPS S *2p* spectrum of a xanthylated surface (binding energy ≈ 165 eV). The peak around 170 eV could correspond to a group containing sulfur in higher oxidation states (30), possibly resulting from the oxidation of the xanthate ester group. *Bottom Right*: XPS Cl *2p* spectrum of a chlorinated surface.

We note that such a photochemical Ritter amidation reaction involving only Selectfluor and nitriles has not been previously reported for small molecule substrates (*SI Appendix*, Fig. S32). By contrast, similar approaches were shown to be effective for functionalization of diamondoids (44) and nanodiamonds (45–47). These results further highlight a difference in the reactivity of high-quality, single-crystal diamond surfaces compared with other structurally analogous diamonds.

We next demonstrated that our surface functionalization strategy is compatible with shallow NV centers with long spin coherence. It has been widely established that coherence properties of

single NV centers depend sensitively on surface termination and morphology (9, 12, 13, 48). Following previous work (12), we prepared smooth and low-defect oxygen-terminated surfaces, introduced nitrogen via ion implantation, and annealed to form NV centers. Next, the samples were hydrogen terminated and subsequently subjected to surface functionalization reactions. It has been observed that hydrogen atom diffusion during hydrogen termination can lead to NV center passivation (49). To address these challenges, we explored three methods of hydrogen termination, including two plasma-based techniques and annealing in forming gas (*SI Appendix, Materials and Methods*). While all three methods

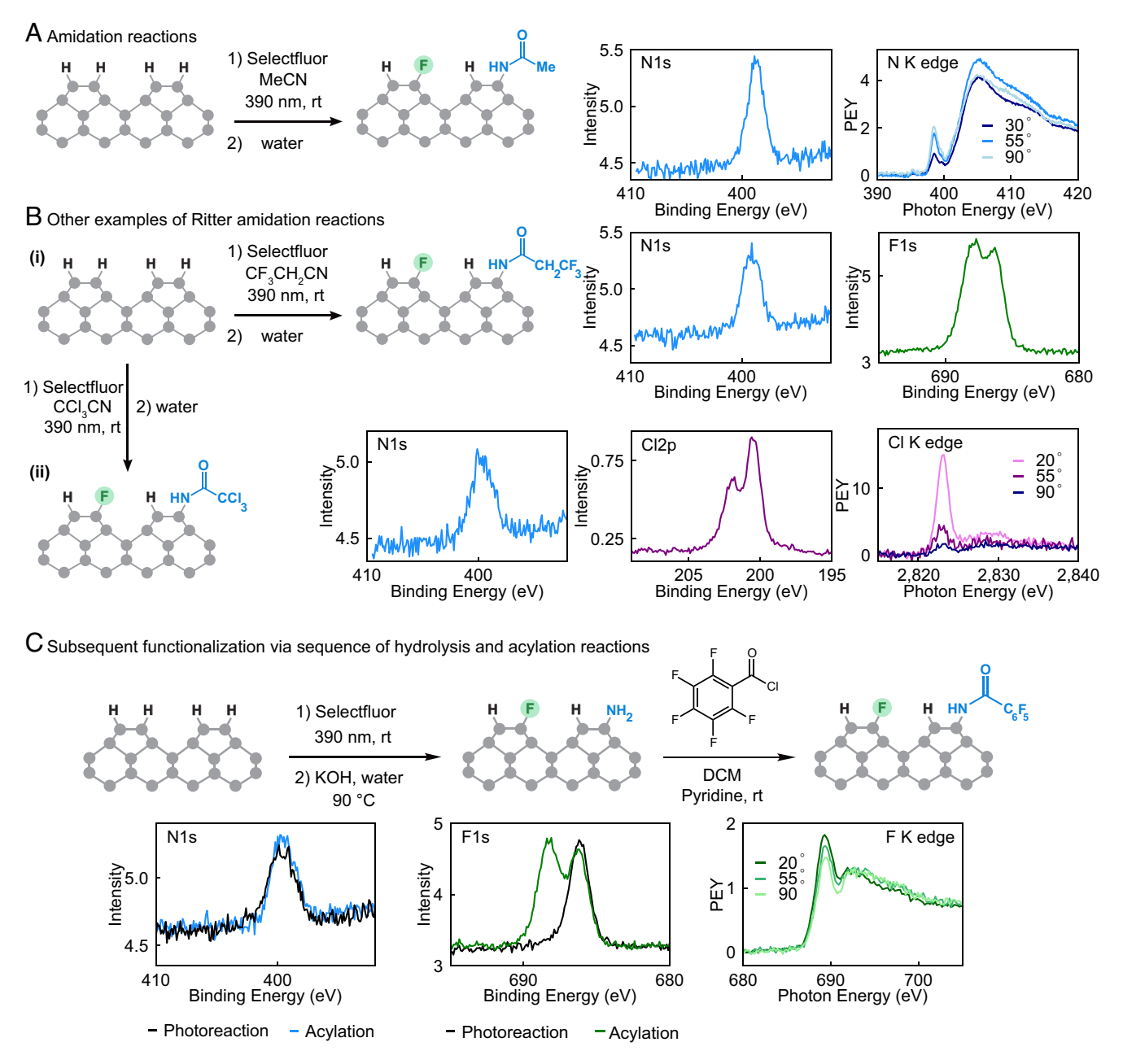


Fig. 3. Amidation of diamond surfaces via a photochemical Ritter reaction. (A) *Left*: Control experiment scheme for the fluorination reaction in the absence of the TBADT photocatalyst leading to the identification of C–N bond formation at the surface. *Middle*: XPS N 1 s spectrum of post-irradiation surface. *Right*: NEXAFS N *K*-edge spectra acquired at different incident X-ray angles relative to the surface after functionalization. The observed angle dependence indicates that the nitrogen groups are well-oriented on the surface, consistent with covalent C–N bond formation. (*B*) Examples of amidation reactions with halogenated nitrile nucleophiles. (*i*) *Left*: Reaction scheme for surface amidation with 3,3,3-trifluoropropionitrile. *Middle*: XPS N 1 s spectrum. *Right*: XPS F 1s spectrum indicating the presence of both C_(diamond)–F bonds (686 eV) and the trifluoromethyl group (CF₃) in the amide (689 eV) (36). (*ii*) *Left*: Reaction scheme for surface amidation with trichloroacetonitrile. *Middle Left*: XPS N 1s spectrum. *Middle Right*: XPS Cl 2p spectrum indicating the presence of trichloromethyl groups on the surface. *Right*: NEXAFS Cl *K*-edge spectra acquired at different incident X-ray angles relative to the surface bearing trichloroacetamide groups. (*C*) *Top*: Subsequent surface functionalization via a sequence of hydrolysis and acylation reactions. *Bottom Left and Middle*: XPS N 1s and F 1s spectra after amidation and acylation reactions. *Bottom Right*: NEXAFS F *K*-edge spectra acquired at different incident X-ray angles relative to a surface bearing pentafluorobenzamide groups.

produced appreciable hydrogen surface coverage (*SI Appendix*, Fig. S1), annealing under forming gas was the only method that was reliably compatible with shallow NV centers. Forming gas annealing does not produce significant quantities of atomic hydrogen that can diffuse readily in the diamond lattice and passivate NV centers or lead to Fermi-level pinning (49). Furthermore, it does not etch the surface and therefore does not etch away shallow NV layers or result in observable changes in surface morphology, which is a proxy for surface damage (*SI Appendix*, Figs. S4 and S5). Additionally, it is well-known that hydrogen termination of

diamond can lead to charge transfer to surface adsorbates, resulting in band bending that destabilizes the NV⁻ charge state (9). This band-bending depends on the surface chemistry, nature of surface adsorbates, and dopant concentration. In this work, we empirically observed that processing with either oxidizing acids or a low-temperature oxygen anneal was helpful to stabilize the NV⁻ charge state after surface functionalization without removing functional groups (*SI Appendix*, Fig. S35).

We studied the impact of surface functionalization on NV center performance by measuring the spin coherence properties

of shallow NV centers under the modified surfaces. We prepared three samples: Samples 1a and 1b were cut from the same larger diamond and processed together to produce "triacid cleaned" surfaces with a disordered oxygen termination (12). Sample 1a was interrogated under this oxygen termination, and Sample 1b was subjected to additional hydrogen termination followed by fluorination under our photochemical conditions prior to measurement. Sample 2 was amidated with 3,3,3-trifluoropropionitrile (more sample information in SI Appendix, Materials and Methods). For all samples, we measured the Hahn echo coherence time (T2) as well as the depth (50) for a random selection of NV centers and observed coherent NV centers within 10 nm of the surface. To benchmark the impact of surface noise on NV properties, we compared the measured T₂ as a function of NV depth (Fig. 4A). We found that the spin coherence times for NV centers in Sample 1b were slightly improved compared to Sample 1a, suggesting the functionalization procedure did not cause significant additional surface damage. The improvement in coherence properties between the triacid cleaned and functionalized samples is comparable to the improvement after previously reported high-purity oxygen annealing (12). We also probed the spectral density of the noise bath using CPMG and XY-8 dynamical decoupling sequences (51). In some cases, we were able to extend the coherence time to 79.7 μ s \pm 4.3 μs for a NV center with a depth of 8.3 nm ± 0.9 nm, demonstrating shallow NV centers with coherence properties comparable to the state of the art (e.g. 127.7 μ s ± 9.5 μ s for a NV center with a depth of 7.5 nm \pm 0.3 nm) (12) under functionalized surfaces (Fig. 4B). We note that some properties of shallow NV centers are worse for functionalized samples than for state-of-the-art surfaces, including shorter double quantum and single quantum lifetimes (T₁) (SI Appendix, Fig. S38), reduction of T₂ after long exposure to green laser illumination, and changing optically detected electron spin resonance (OD-ESR) contrast under green laser illumination (SI Appendix, Fig. S39). Improving these parameters is an important subject for future work.

The shallow NV center properties we observed enable the detection of excess noise arising at the Larmor frequency of nuclear spins within the functional groups attached to the surface. We demonstrated this functionality using ensembles of shallow NV centers as a proof-of-principle experiment. The ensemble samples were prepared by implanting with a higher dose of 15 N (2.5 keV, 2 × 10) ions/cm²) and annealing to form NV centers. We found that the dynamically decoupled coherence properties of the ensemble samples were slightly improved after functionalization (Fig. 4C) and that our OD-ESR readout contrast was largely preserved (SI Appendix, Fig. S42). This slight improvement may arise from reduced disorder in the surface terminated with a mixture of hydrogen, fluorine, and oxygen relative to the fully oxygen-terminated surface, which has been established to comprise a number of different oxygen species (12, 52). However, we did observe a reduction in the double quantum T₁ (SI Appendix, Fig. S43) and that the OD-ESR contrast and charge state properties of NV centers depend sensitively on the environment and time under green laser illumination (SI Appendix, Fig. S41).

We used these ensemble samples to detect the statistical polarization of ^{19}F nuclear spins attached to the surface. These nuclear spins precess at the Larmor frequency determined by their gyromagnetic ratio and the applied magnetic field, generating an AC magnetic signal, which can be detected using correlation spectroscopy (Fig. 4D) (53, 54). In this experiment, the NV center is driven with an XY-8 pulse sequence that flips the NV center synchronously with the Larmor frequency of the ^{19}F signal. The NV center accumulates phase due to noise arising from ^{19}F nuclear spins during an initial XY-8 block. After this block, a $\pi/2$ pulse

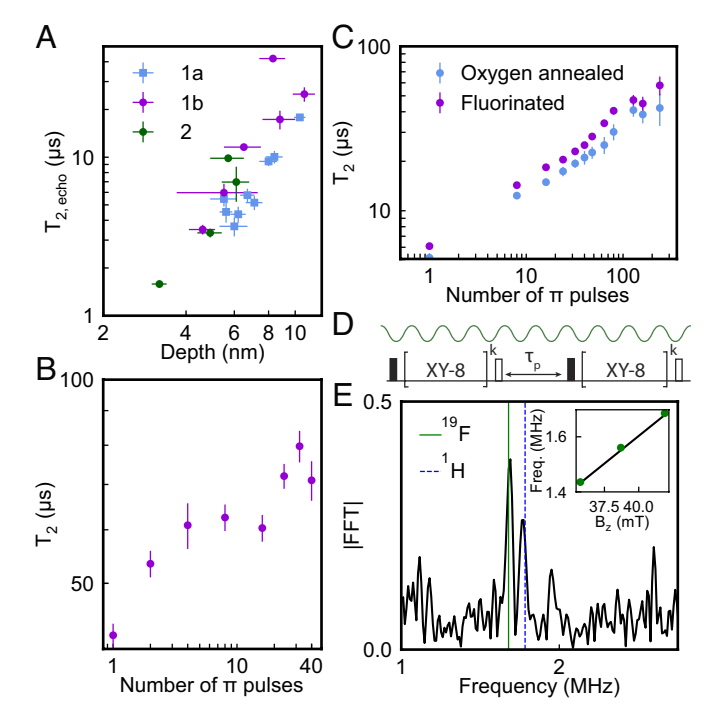


Fig. 4. NV sensors under functionalized surfaces. (A) Hahn echo coherence time (T_{2, echo}) as a function of NV center depth under functionalized surfaces. Samples 1a and 1b are pieces of the same diamond that was implanted and processed before dicing. Sample 1a was characterized under an "acid cleaned" oxygen terminated surface (12), while Sample 1b was hydrogen terminated followed by fluorination and acid cleaning. Sample 2 was functionalized using the Ritter reaction with 3,3,3-trifluoropropionitrile and subjected to a lowtemperature oxygen anneal. (B) Coherence times with dynamical decoupling for a single 8.3 nm \pm 0.9 nm deep NV center in Sample 1b. Increasing the number of π pulses extends the coherence time to 79.7 μ s \pm 4.3 μ s. (C) Dynamically decoupled coherence times for a shallow NV ensemble in Sample 3 as a function of the number of π pulses. The same sample is interrogated after oxygen annealing and subsequent fluorination. (D) Diagram of the NV-NMR sensing sequence. The green wave depicts an oscillating magnetic field from nuclear spins. The black pulse diagram shows the correlation sequence used to detect nuclear spins. Two XY-8 blocks allow the NV center to accumulate phase from ¹⁹F nuclear spins. Each block is repeated k times. The black and white blocks represent $\pi/2$ pulses around orthogonal axes. The time between the blocks, τ_p , is scanned during the experiment. (E) Fourier transform of correlation sequence data (*SI Appendix*, Fig. S44) reveals a peak at the expected frequency for ¹⁹F at a magnetic field of 42 mT, arising from covalently attached fluorine. This dataset was acquired by averaging the time domain signal for 10 spots on the sample over 5 h and has a signal to noise ratio of around 10. The magnetic field dependence of the peak position is consistent with the gyromagnetic ratio of ¹⁹F (*Inset*).

stores the phase information in the amplitude of the NV center. After a delay time (τ_p) , a second phase accumulation block occurs. Scanning the time between the two-phase accumulation blocks leads to a signal that oscillates at the Larmor frequency of the nuclear spins.

We performed this experiment on Sample 3, which was fluorinated using TBADT and Selectfluor, and detected the magnetic signal associated with ¹⁹F. To optimize photon collection efficiency while reducing the proton background, the samples were mounted in deuterated propylene carbonate (*SI Appendix, Materials and Methods*). We repeated the XY-8 sequence five times (k = 5) to optimize sensitivity while suppressing the proton signal. Taking the Fourier transform of this trace (*SI Appendix*, Fig. S44) showed a peak at the ¹⁹F frequency (Fig. 4E). The power spectrum of the ¹⁹F NMR peak has a linewidth of 25.44 kHz ± 2.02 kHz, which is similar to previously measured linewidths of protons in polymers (53) and surface-bound fluorine groups (7) (*SI Appendix*, Fig. S48). To verify that the signal arose from ¹⁹F, we swept the magnetic field and observed a shift in peak frequency consistent with the

gyromagnetic ratio of ¹⁹F (Fig. 4 *E, Inset*, also see *SI Appendix*, Fig. S45). Finally, we repeated the same experiment for a nonfunctionalized sample and did not detect a ¹⁹F signal, confirming the absence of spurious signals from unintentional fluorine contamination sources (SI Appendix, Fig. S47).

Outlook

Here, we have demonstrated a photochemical strategy to directly functionalize high-quality, single-crystal diamond surfaces that enables the covalent attachment of sensing targets for NV-based NMR sensing. The method relies on the HAT activation of inert C–H bonds to generate highly reactive free radical and carbocation intermediates, which engage in a range of bond-forming reactions to install diverse functional groups with surface coverage up to 10% (1.6 molecules/nm²) under mild conditions. This density of functional groups is a suitable grafting density for attachment of proteins for single-molecule studies (55). An important avenue for future work may be to controllably lower the density, by altering the choice of reagent or reaction conditions. More broadly, we have developed a reaction discovery pipeline using multimodal spectroscopic characterization that is readily generalizable to other classes of chemistry. Notably, we have shown that our surface functionalization strategy is compatible with coherent shallow NV centers and we use NV centers to detect the Larmor precession of ¹⁹F spins that are covalently attached to the diamond surface. Future work includes further diversifying the scope of functionalization reactions, in particular attaching biomolecules, such as proteins and nucleic acids, to enable nanoscale NMR studies. A further goal will be to establish that biomolecules and other sensing targets retain their functionality upon attachment to the surface and remain stable under optical and microwave excitation conditions during sensing experiments. An interesting avenue is to explore whether this lightdriven functionalization approach can be used to colocate NV centers with sensing targets, perhaps through a FRET-based functionalization scheme involving excitation by NV fluorescence. Combining with advances in sensing protocols (56, 57) or biophysical techniques (58), this experimental capability has the potential to probe the magnetic signature of small ensembles of biomolecules, down to the single-molecule regime, enabling novel studies of dynamic structural changes in individual biomolecules.

Materials and Methods

General Information.

Sample preparation for reaction discovery. All diamond samples in this work were purchased from Element Six and are single crystal samples grown by chemical vapor deposition. Standard-grade samples with (100) surfaces were used for reaction discovery and testing different hydrogen termination procedures. These samples were prepared with smooth surfaces following previous work (12) prior to being subjected to various hydrogen termination and functionalization procedures. For the purposes of reaction discovery, we treat the hydrogen-terminated surface as the starting condition before subjecting samples to reactions.

Surface spectroscopy measurement details. XPS data were acquired at normal incidence using a Thermo Fisher K-Alpha XPS and X-ray spectrometer tool with an aluminum anode (1,486.8 eV) and a 250 µm spot size. A flood gun was used to mitigate issues with sample charging. All XPS data were processed by shifting the binding energy based on C 1s sp³ reference (284.8 eV) and normalized to the sum of the total signal collected in the survey scan to account for focusing variation. This tool did not have the capability to perform in situ annealing so contributions of adventitious carbon and water from the atmosphere are expected to contribute to C 1s and O 1s signals.

All AFM images were taken with a Bruker Icon3 tool operating in tapping mode (AFM tip from Oxford Instruments Asylum Research, part number AC160TS-R3, resonance frequency 300 kHz). Error values for average roughness (R_a) were computed by dividing the image into quadrants, computing the Ra for each quadrant, and then calculating the SD of those values.

LEED images were acquired using a OCI Vacuum BDL-450 w/ Z-translation (190 mm + 10 mm WD) installed in a custom ultra-high vacuum chamber. The spectra in this work were collected with approximately 252 eV beam energy.

NEXAFS spectra were collected using the polarized soft X-ray sources at both the Australia Synchrotron as well as the SST-1 and SST-2 beamlines at NSLS-II, Brookhaven National Lab. In all cases, the data were collected in partial electron yield (PEY) mode. A flood gun was used to mitigate sample charging.

The N K-edge measurements shown in Fig. 3A and SI Appendix, Fig. S20 and the F K-edge measurements shown in Fig. 2B and SI Appendix, Figs. S10 and S20 were collected at the Australia Synchrotron in the high-throughput system. This system had a base pressure of 10^{-7} mbar and used a retarding grid detector. The retarding grid bias was set to -100 V and -550 V for N and F K-edge measurements, respectively. The C K-edge measurements shown in SI Appendix, Fig. S2 were collected at the Australia Synchrotron in the Prevac endstation with a base pressure of 10^{-10} mbar.

For SST-1 and SST-2 measurements, data were collected using channeltron electron multipliers. Energy selection was accomplished using a variable line spacing plane grating monochromator at SST-1 and a double Si (111) crystal monochromator at SST-2. The N K-edge and O K-edge measurements shown in SI Appendix, Fig. S30 were collected at SST-1 with the entrance grid bias set to -280 V and -400 V, respectively. The F K-edge and C K-edge measurements shown in Fig. 3C in the main text and SI Appendix, Fig. S35 were collected at SST-1 with an entrance grid bias of -550 V and -150 V, respectively. All Cl K-edge measurements shown in this work were collected at SST-2 and the entrance grid bias set between -1,800 V and -2,000 V.

The NEXAFS data were processed by first normalizing to the total intensity of the incident beam which was measured by the drain current off a gold grid (I_0) . Data acquired at the Australia Synchrotron were "double normalized" to a signal from a photodiode in the end chamber after dividing the photodiode signal by the corresponding I₀. Next, the average value of the PEY signal from the pre-edge region was subtracted. For some datasets, the pre-edge PEY signal was fit to a linear function and this was subtracted instead of the mean value. Finally, the data were normalized to the average PEY signal in the post-edge region. Photon energy for datasets acquired at SST-1 were shifted based on a reference energy calibration. Photon energy for datasets acquired at the Australia synchrotron were shifted based on C K-edge features (sp² peak, diamond exciton peak) such that they aligned with SST-1 datasets that were shifted based on the measured energy reference. Cl K-edge datasets acquired at SST-2 were not shifted.

Hydrogen-Terminated Diamond Surface Preparation. In this work, three methods of hydrogen terminating (100) diamond surfaces were used. Details of surface characterization for samples prepared with the different methods can be found in SI Appendix.

"As grown" plasma. The samples were processed in a CVD diamond growth chamber. Notably, this procedure etches and regrows the top few microns of material. The procedure has been described previously (13), but we provide a brief description for completeness. Diamond growth and termination was conducted in a "clamshell" type Seki reactor (Seki SDS 6500 with a palladium-based hydrogen purifier) under a hydrogen plasma at 85 Torr (1.1 \times 10⁴ Pa) and 4,500 W. The growth step consisted of exposure to 4% methane for 5 min followed by a hydrogen termination step (no methane addition) for about 3 min with microwave power decreased to 3,200 W. The sample temperature is approximately 700 °C at plasma extinction.

"Gentle" plasma. The goal of this procedure was to use a plasma to gently terminate the surface without etching or removing material. The termination was done in a SEKI AX6300 chemical vapor deposition diamond growth chamber with a base pressure of 2 \times 10 $^{-6}$ Pa. After loading the sample, the hydrogen plasma was initiated with an RF power of 750 W and a flow rate of 400 sccm and a corresponding pressure of 25 Torr (3.3 \times 10³ Pa). Over a duration of 5 min, the sample temperature was gradually elevated to 800 °C. Subsequently, the sample was held at 800 °C for (15 to 50) min before undergoing a controlled temperature reduction to 200 °C over a period of 20 min. To mitigate hydrogen dissociation during the cooling process, the plasma settings were adjusted to a reduced RF power of 400 W, a flow rate of 30 sccm, and a pressure of 3.5 Torr (0.5 \times 10³ Pa). The plasma was deactivated upon reaching the target temperature of 200 °C following a 20-min cool-down period.

Hydrogen annealing. Adapted from literature reports of producing hydrogenterminated single crystal diamond by annealing under pure hydrogen gas (59), hydrogen-terminated diamonds were produced by annealing under an atmosphere of forming gas (5% H₂, 95% Ar, Airgas X02AR95C3000993) in a tube furnace (Thermo Scientific Lindberg/Mini Mite). This same procedure was used in another recent work (60). The sample was heated to 100 °C over 1 h, held at 100 °C for 2 h for degassing, ramped to 800 °C over 2.5 h, and held at 800 °C for 72 h. In the course of developing this procedure, annealing durations ranging from 24 h to 2 wk were used with similar results. The majority of the samples in this work were annealed for 72 h for consistency. The setup consisted of a tube furnace with a quartz tube, a mass flow controller to control the flow rate, and a bubbler with mineral oil at the output of the furnace to isolate the chamber from atmosphere. The forming gas was filtered before entering the furnace (SAES MC1-203F). The samples were loaded in a high-purity alumina boat purchased from CoorsTek.

Cleaning Procedures for Post-Functionalization Diamond Samples. A key challenge with using XPS for reaction discovery is that insufficient cleaning after the reaction can lead to spurious XPS results arising from nonspecific binding (SI Appendix, Fig. S6). We addressed this issue by developing a thorough cleaning procedure to remove contamination while leaving surface-bonded functional groups intact. Typically, samples were first sonicated in the solvent of the reaction, heated them to 50 °C in dimethyl sulfoxide (DMSO) for 1 h, and then sonicated them for 20 min in each of the following: N-methylpyrrolidone (NMP) or DMSO, chloroform, deionized (DI) water, acetone, and isopropyl alcohol (IPA). This solvent sequence was adjusted based on the stability of various functional groups. XPS was then used to check for the presence of the heteroatom associated with a particular functional group and the absence of other contaminants from the reaction (SI Appendix, Figs. S7 and S8). Additionally, since physisorbed contaminants rarely result in an evenly distributed monolayer, AFM was used to survey dried contamination on the surface (SI Appendix, Fig. S9). The cleaning procedure and surface analysis were routinely repeated to check for consistency in the XPS results through several cleans.

Surface Functionalization Reactions.

General information. Purple Kessil lamps used in this work are Kessil H150B LED Grow Light (390 and 456 nm) purchased from Kessil. All reactions were carried out in well-ventilated fume hoods. Gas chromatography (GC) was performed on an Agilent Technologies 7890A GC system equipped with a split-mode capillary injection system and flame ionization detectors. N-(tert-butyl)-N-chloro-3,5bis(trifluoromethyl)benzamide and N-(tert-butyl)-N- ((ethoxycarbonothioyl) thio)-3,5-bis(trifluoromethyl)benzamide reagents that were used in chlorination and xanthylation reactions were synthesized according to previous reports (31, 32). Other reagents and solvents are commercially available.

Photochemical fluorination reaction procedure. A hydrogen-terminated, single-crystal diamond sample (2 mm × 2 mm) was added to a 1-dram vial along with a magnetic stir bar, tetra-n-butylammonium decatungstate (10 mg), and the fluorinating reagent (e.g., N-fluorobenzenesulfonimide (NFSI) or Selectfluor) (100 mg). The reaction mixture was degassed and backfilled with argon three times, after which 0.5 mL of dry acetonitrile was added. The reaction was then stirred at room temperature for 48 h under the irradiation of 390 nm purple Kessil lamps and kept near room temperature using fans. At the end of the reaction, the diamond sample was thoroughly washed using the cleaning procedure described above and dried using a nitrogen spray gun before characterization.

Chlorination reaction procedure. A hydrogen-terminated, single-crystal diamond was added to a 2-dram vial along with a magnetic stir bar, N-(tert-butyl)-N-chloro-3,5-bis(trifluoromethyl)benzamide (50 mg), and cesium carbonate (47 mg). The reaction mixture was degassed and backfilled with argon three times, after which 0.4 mL of anhydrous benzene was added. The reaction was then stirred for 24 h under the irradiation of 456 nm blue Kessil lamps. The reaction temperature was maintained at approximately 65 °C over the course of the reaction by the heat produced by the lamps; no fans were used. At the end of the reaction, the diamond sample was thoroughly washed using the cleaning procedure described above and dried using a nitrogen spray gun before characterization.

Xanthylation reaction procedure. A hydrogen-terminated, single-crystal diamond was added to a 2-dram vial along with a magnetic stir bar and N-(tertbutyl)-N-((ethoxycarbonothioyl)thio)-3,5-bis(trifluoromethyl)benzamide (170 mg). The reaction mixture was degassed and backfilled with argon three times, after which 0.4 mL of anhydrous trifluorotoluene was added. The reaction was then stirred at room temperature for 24 h under the irradiation of 456-nm blue Kessil lamps. The reaction temperature was maintained near room temperature over the course of the reaction using fans. At the end of the reaction, the diamond sample was thoroughly washed using the cleaning procedure described above and dried using a nitrogen spray gun before characterization.

Photochemical procedure for C-N bond formation. A hydrogen-terminated, single-crystal diamond sample (2 mm × 2 mm) was added to a 1-dram vial along with a magnetic stir bar and Selectfluor (100 mg). The reaction mixture was degassed and backfilled with argon three times, after which 0.4 mL of degassed nitrile reagent was added. Examples of nitrile reagents include acetonitrile, trichloroacetonitrile, and 3,3,3-trifluoropropanetrile. The reaction was then stirred at room temperature for 48 h under the irradiation of 390 nm purple Kessil lamps and kept near room temperature using fans over the course of the reaction. At the end of the reaction, the diamond sample was thoroughly washed using the cleaning procedure described above and dried using a nitrogen spray gun before characterization.

Hydrolysis reaction procedure. A diamond sample with an amide-terminated surface, which was obtained after the Ritter reaction, was added to a 2-dram vial along with a magnetic stir bar and potassium hydroxide (56 mg). DI water (0.4 mL) was added and the reaction mixture was stirred under an inert atmosphere at 90 °C for 24 h. At the end of the reaction, the diamond sample was thoroughly washed using the cleaning procedure described above and dried using a nitrogen spray gun before characterization.

Acylation reaction procedure. A diamond sample with an amine-terminated surface, which was obtained after the hydrolysis reaction, was added to a 2-dram vial along with a magnetic stir bar. The vial was then degassed and backfilled with Ar three times. Next, anhydrous dichloromethane (0.3 mL), pyridine (30 µL), and acylation reagent (0.1 mL) were added. The vial was then sealed, placed under an inert atmosphere, and stirred at room temperature for 24 h. At the end of the reaction, the diamond sample was thoroughly washed using the cleaning procedure described above and dried using a nitrogen spray gun before characterization. Examples of acylation reagents include pentafluorobenzoyl chloride, 3,5-bis(trifluoromethyl) benzoyl chloride, and heptafluorobutyric anhydride (SI Appendix, Fig. S28).

Additional Processing for Samples Containing NV Centers. "Triacid clean": the sample was subjected to a refluxing mixture of sulfuric, perchloric, and nitric acids in a 1:1:1 volumetric ratio for 2 h.

Low temperature oxygen anneal: Samples were placed in a tube furnace and subjected to high-purity oxygen gas. The furnace was first to 100 °C over 1 h, held at 100 °C for 2 h for degassing, ramped to 300 °C over 2 h, and held at 300 °C for 3.5 h before shutting off the furnace.

Single NV Center Measurements.

Single NV measurement details. The details of our single NV measurement setup have been published elsewhere (12, 61). Single NV center measurements were performed on a home-built confocal microscope (SI Appendix, Fig. S37). NV centers are excited by a 532 nm optically pumped solid state laser (OPSL, Coherent Sapphire) which is modulated with an acousto-optic modulator (AOM). The beam is scanned using galvo mirrors and projected into an oil immersion objective (Nikon, Plan Fluor 100×, NA = 1.30) with a telescope in a 4f configuration. Laser power at the back of the objective was kept between (60 to 100) μ W, approximately 25% of the saturation power of a single NV center, in order to avoid irreversible photobleaching. A dichroic beamsplitter separates the excitation and collection pathways, and fluorescence is measured using a fiber-coupled avalanche photodiode (Excelitas SPCM-AQRH-44-FC). A neodymium permanent magnet was used to introduce a DC magnetic field for Zeeman splitting and the orientation of the magnetic field was aligned to within 1° of the NV center axis using a goniometer.

Spin manipulation on the NV center was accomplished using microwaves. The output of a signal generator was gated with fast SPDT switches (Mini-Circuits ZASWA-2-50DR+) before being amplified by a Mini-Circuits amplifier (ZHL-16-W-43+). The signal was then delivered to the sample via a coplanar stripline. The stripline was fabricated by depositing 10 nm Ti, 1,000 nm Cu, and 200 nm Au on a microscope coverslip at a commercial facility. Following metallization, the stripline was photolithographically defined and etched with gold etchant and hydrofluoric acid. Finally, a 100 nm layer of Al₂O₃ was deposited on top of the fabricated stripline via atomic layer deposition (ALD) to protect the metal layer. Pulse timing was controlled with a Spincore PulseBlaster ESR-PRO500 with 2 ns timing resolution.

Coherence time measurements for samples 1a and 1b were collected at 190 mT and NV depth measurements were performed around 27 mT. Coherence time and depth measurements for Sample 2 (12C enriched) were collected at 46 mT. For all samples, depth measurements were estimated using the NMR proton signal from microscope immersion oil, following the protocol outlined in previous work (50). The dataset shown in Fig. 4B used the CPMG sequence for (1 to 4) π pulses and the XY-8 sequence for (8 to 40) π pulse measurements. Double quantum and single quantum lifetime (T_1) measurements were conducted at low field (3 mT). Single NV center sample preparation. All samples were purchased or obtained from Element Six.

Sample 1a: An electronic grade single crystal (denoted as ELSC by Element Six) grade sample purchased from Element Six with a natural abundance of ¹³C nuclear spins. The sample was implanted with a low density of ¹⁵N (3 keV, 10⁹/cm², 0° tilt) and annealed to form NV centers. Prior to measurement, the sample was oxygen annealed and then "reset" with another 800 °C anneal in a vacuum tube furnace. The activation, oxygen, and reset anneals followed procedures outlined in previous work (12). The activation and reset annealing procedures produce NV centers with comparable coherence properties (12).

Sample 1b: An ELSC grade sample cut from the same larger diamond as Sample 1a. The two samples were implanted with the same ion implantation parameters and processed together (subjected to activation anneal, oxygen anneal, reset anneal). The sample was then subjected to anneal in forming gas (24 h anneal) followed by the direct fluorination reaction and an acid clean.

Sample 2: An ELSC grade sample with an isotopically purified ¹²C layer. The surface was "as grown" (i.e., was not subjected to polishing or etching). This sample was implanted with low dose ¹⁵N ions to form single NV centers (1.5 keV, 10⁹/ cm², 0° tilt) and annealed in a vacuum tube furnace to 800 °C to form NV centers. The sample was then subjected to a 72 h anneal in forming gas, functionalized using the Ritter reaction with 3,3,3-trifluoropropionitrile, and then subjected to a low-temperature oxygen anneal prior to NV measurements.

NV Ensemble Measurements.

Ensemble measurement details. A home-built single-center scanning confocal microscope was modified for wide-field ensemble measurements (SI Appendix, Fig. S40). This allowed the excitation of a large number of NV centers at once, boosting the sensitivity for proof-of-principle sensing experiments. Most notably, ensemble experiments require higher laser power, a change in optics to excite a large spot size, and a different type of photodetector that can detect higher amounts of fluorescence.

NV centers were excited using a 532 nm green laser (Lighthouse Photonics, Sprout-H-5 W). The laser output was set to 1 W, which corresponded to approximately 300 mW before the dichroic. The diameter of the laser beam was reduced with a telescope before entering the AOM. After the AOM, a polarizer was used to rotate polarization to maximize the NV signal from the NV centers that are aligned along the magnet axis. Next, a telescope expanded the beam and the beam width was adjusted based on the desired spot size on the diamond. An iris was placed at the focal plane of the first telescope lens to spatially reject the other modes of the AOM. The aperture of this iris was adjusted to allow for an appropriate extinction ratio, following previous widefield experiments (62). Next, a lens focused the green laser on the back focal plane of the objective. The distance between this lens and the objective was adjusted such that the light coming out of the objective was approximately collimated. The spot size on the sample is determined by the beam diameter going into the focusing lens, the length of the focusing lens, and the effective focal length of the objective. In our setup, the spot size can be most easily tuned by changing the telescope lenses before the focusing lens. NV fluorescence was collected by an oil immersion objective with 100× magnification and 1.3 NA (Nikon N100×-PFO) and separated from green excitation by a short pass dichroic (Thorlabs DMSP550). This dichroic was chosen to reflect both NV⁰ and NV⁻ fluorescence. Microscope immersion oil (Nikon, Type N) was used between the objective and coverglass and the front aperture of the objective was routinely cleaned. In the collection path, a removable mirror mount allowed emission from both charge states to be studied on a spectrometer by passing the emission through a 532 nm notch filter (Semrock NF03-532E-25) onto a reflective collimator with a fiber coupler. This proved useful for troubleshooting charge state changes under green laser illumination. With the mirror mount removed, the emission was focused onto an analog photodetector (Thorlabs APD410a). Before the photodetector, a 532 nm notch filter (Semrock NF03-532E-25) and a 647 nm

long pass filter (Semrock BLP01-647R-25) removed remaining green excitation and filtered out NV⁰ emission. The output of the photodetector was connected to an analog input of a DAQ (National Instruments, PXIe-6363) for readout. The readout approach and optimization followed the methodology outlined in previous widefield experiments (62).

Microwave spin manipulation as well as experiment timing and control was accomplished using the same hardware used in single NV measurements.

Ensemble coherence time measurements were acquired at a bias magnetic field around 41 mT. The dataset shown in Fig. 4C used the Hahn echo CPMG sequence for one π pulse and the XY-8 sequence for (8 to 240) π pulse measurements. ¹⁹F NMR sensing experiments were performed between 35 mT and 42 mT. Lifetime (T₁) measurements were conducted at low field (approximately 3 mT). NV ensemble sample preparation. All samples were purchased or obtained from Element Six.

Sample 3: An ELSC sample that was cut from the same diamond as Sample 2 after low density ion implantation and activation annealing. Next, the sample was implanted with higher dose (2.5 keV, 2×10^{12} /cm², 7° tilt) and annealed to 800 °C in a vacuum tube furnace to form NV centers. The sample was then oxygen annealed following the procedure established in previous work (12), hydrogen annealed, and subjected to the direct fluorination reaction.

Sample 4: An ELSC grade sample with an isotopically purified ¹²C layer. The surface was "as grown" (i.e., was not subjected to polishing or etching). This sample was implanted with low dose ¹⁵N ions to form single NV centers (1.5 keV, 10⁹/ cm², 0° tilt) and annealed to form NV centers. Next, the sample was implanted at a higher dose (2.5 keV, 2×10^{12} /cm², 7° tilt) and annealed to 800 °C in a vacuum tube furnace to form NV centers.

NV-NMR Experiment. NV-NMR experiments were performed with the sample mounted in deuterated propylene carbonate (Cambridge Isotopes DLM-1279-1). This was chosen because it has a similar index of refraction to oil, led to favorable NV charge state properties (SI Appendix, Fig. S41), did not cause fluorescence features that overlapped with the NV spectrum of interest, and is commercially available in deuterated form. Furthermore, the deuterated solvent helps to reduce the background proton signal. Since proton and fluorine nuclear spins have similar gyromagnetic ratios, their signals appear near each other in an NMR spectrum. In this experiment, the goal was to detect a small fluorine signal from our functionalized layer, so it was helpful to minimize the background proton signal.

Data were collected by scanning the free precession time (τ_n) from 256 ns to 32.256 µs in 800 steps. Example time domain data are shown in SI Appendix, Fig. S44. For the data shown in the main text (Fig. 4E), the data were zero filled out to $96.256 \,\mu s$ prior to taking the fast Fourier transform (FFT). The time in between π pulses within XY-8 blocks for the data shown in main text Fig. 4E was 296 ns.

The signal-to-noise ratio (SNR) is calculated by finding the amplitude of the datapoint nearest to the expected fluorine frequency, subtracting the baseline, and dividing by the SD of the noise floor. The NMR dataset shown in the main text (Fig. 4E) had an SNR of 13 before zero filling and 9 after zero filling.

Disclaimer. Certain commercial equipment, instruments, or materials are identified in this paper in order to specify the experimental procedure adequately, and do not represent an endorsement by the National Institute of Standards and Technology.

Data, Materials, and Software Availability. All study data are included in the article and/or SI Appendix.

ACKNOWLEDGMENTS. We thank Peter Maurer for helpful discussions, Zihuai Zhang for help with experimental challenges, and Zeeshawn Kazi for help with data analysis. This work was primarily supported by the Princeton Catalysis Initiative and the U.S. Department of Energy, Office of Science, Office of Basic Energy Sciences, under Award No. DE-SC0018978. The surface processing and spectroscopy pipeline was supported by the NSF CAREER program Grant No. DMR1752047, ensemble NMR and single center sensing were supported by the NSF Grant No. OMA-1936118, and some surface functionalization was supported by the Center for Molecular Quantum Transduction, an Energy Frontier Research Center funded by the U.S. Department of Energy, Office of Science, Office of Basic Energy Sciences, under Award No. DE-SC0021314CMQT. L.V.H.R. acknowledges support from the Department of Defense through the National Defense Science and Engineering Graduate Fellowship Program. J.H.C. acknowledges the NSF for a Graduate Research Fellowship (Grant No. #DGE-2039656). This research used resources of the Spectroscopy Soft and Tender Beamlines (SST-1 and SST-2) operated by the National Institute of Standards and Technology, located at the National Synchrotron Light Source II. NSLS-II is operated by the U.S. Department of Energy Office of Science Facilities at Brookhaven National Laboratory under contract no. DE-SC0012704. We acknowledge the use of Princeton's Imaging and Analysis Center (IAC), which is partially supported by the Princeton Center for Complex Materials (PCCM), a NSF Materials Research Science and Engineering Center (MRSEC; DMR-2011750. This research was partly undertaken on the Soft X-ray Spectroscopy beamline at the Australian Synchrotron, part of ANSTO. S.A.M., L.B.H., and A.C.B.J. gratefully acknowledge support from the US Department of Energy (BES Grant No. DE-SC0019241), as well as the use of shared facilities at the UCSB Quantum Foundry through the Q-AMASE-i program (Grant No. NSF DMR-1906325). L.B.H. acknowledges the support from the NSF Graduate Research Fellowship Program (Grant No. DGE 2139319) and the UCSB Quantum Foundry. S.A.M. acknowledges the support from the UCSB Quantum Foundry. A.G. acknowledges the Hungarian NKFIH Grant No. KKP129866 of the National Excellence Program of Quantum-coherent materials project, the support for the Quantum Information National Laboratory from the Ministry of Culture and Innovation of Hungary (NKFIH Grant No. 2022-2.1.1-NL-2022-00004), the EU EIC Pathfinder project "QuMicro" (Grant No. 101046911), and the EU QuantERA for the project MAESTRO. A.P. also acknowledges the support of Bolyai János Research Fellowship of the Hungarian Academy of Sciences and the computational resources provided by the Governmental Information Technology Development Agency (KIFÜ) of Hungary. S.S. acknowledged funding support from the NSRF via the Program Management Unit for Human Resources & Institutional Development, Research and Innovation (Grant No. B05F650024). Since the submission of this manuscript, some of the data and materials in this manuscript can also be found in the theses of S.T.N. (63) and L.V.H.R. (64).

Author affiliations: ^aDepartment of Electrical and Computer Engineering, Princeton University, Princeton, NJ 08540; ^bDepartment of Chemistry, Princeton University, Princeton, NJ 08540; ^cSchool of Physics, Suranaree University of Technology, Nakhon Ratchasima 30000, Thailand; ^dCenter of Excellence in Advanced Functional Materials, Suranaree University of Technology, Nakhon Ratchasima 30000, Thailand; *Chool of Physics, University of Melbourne, Parkville, VIC 3010, Australia; *School of Science, RMIT University, Melbourne, VIC 3000, Australia; *Materials Measurement Science Division, Material Measurement Laboratory, National Institute of Standards and Technology, Gaithersburg, MD 20899; "HUN-REN Wigner Research Centre for Physics, Institute for Solid State Physics and Optics, Budapest H-1525, Hungary; 'MTA-WFK Lendület "Momentum" Semiconductor Nanostructures Research Group, Budapest H-1525, Hungary; ^jDepartment of Atomic Physics, Institute of Physics, Budapest University of Technology and Economics, Budapest H-1111, Hungary; ^kAustralian Synchrotron, Australian Nuclear Science and Technology Organisation, Clayton, VIC 3168, Australia; Physics Department, University of California, Santa Barbara, CA 93106; and ^mMaterials Department, University of California, Santa Barbara, CA 93106

Author contributions: L.V.H.R., S.T.N., R.R.K., and N.P.d.L. designed research; L.V.H.R., S.T.N., J.H.C., K.Z., Z.Y., S.S., A.S., C.J., C.W., A.P., A.G., L.T., S.A.M., L.B.H., A.C.B.J., X.G., R.J.C., R.R.K., and N.P.d.L. performed research; Z.Y., S.S., A.S., C.J., C.W., L.T., X.G., R.J.C., and N.P.d.L. contributed new reagents/analytic tools; L.V.H.R., S.T.N., J.H.C., K.Z., R.R.K., and N.P.d.L. analyzed data; and L.V.H.R., S.T.N., J.H.C., K.Z., S.S., A.P., A.G., R.R.K., and N.P.d.L.

- J. R. Maze et al., Nanoscale magnetic sensing with an individual electronic spin in diamond. Nature 455, 644-647 (2008).
- I. Lovchinsky et al., Nuclear magnetic resonance detection and spectroscopy of single proteins using quantum logic. Science 351, 836-841 (2016).
- M. S. Grinolds et al., Subnanometre resolution in three-dimensional magnetic resonance imaging of individual dark spins. Nat. Nanotechnol. 9, 279-284 (2014).
- D. R. Glenn et al., High-resolution magnetic resonance spectroscopy using a solid-state spin sensor. Nature 555, 351-354 (2018).
- M. H. Abobeih et al., Atomic-scale imaging of a 27-nuclear-spin cluster using a quantum sensor. Nature 576, 411-415 (2019).
- M. Xie et al., Biocompatible surface functionalization architecture for a diamond quantum sensor. Proc. Natl. Acad. Sci. U.S.A. 119, e2114186119 (2022).
- K. S. Liu et al., Surface NMR using quantum sensors in diamond. Proc. Natl. Acad. Sci. U.S.A. 119, e2111607119 (2022).
- S. Szunerits, C. E. Nebel, R. J. Hamers, Surface functionalization and biological applications of CVD diamond. MRS Bull. 39, 517-524 (2014).
- M. V. Hauf et al., Chemical control of the charge state of nitrogen-vacancy centers in diamond. Phys. Rev. B 83, 081304 (2011).
- 10. S. Cui, E. L. Hu, Increased negatively charged nitrogen-vacancy centers in fluorinated diamond. Appl. Phys. Lett. 103, 051603 (2013).
- J. M. Abendroth et al., Single-nitrogen-vacancy NMR of amine-functionalized diamond surfaces. Nano Lett. 22, 7294-7303 (2022).
- 12. S. Sangtawesin et al., Origins of diamond surface noise probed by correlating single-spin measurements with surface spectroscopy. Phys. Rev. X 9, 031052 (2019).
- A. Stacey et al., Evidence for primal sp ² defects at the diamond surface: Candidates for electron trapping and noise sources. Adv. Mater. Interfaces 6, 1801449 (2019).
- 14. A. Krueger, "Current issues and challenges in surface chemistry of nanodiamonds" in Nanodiamonds, (Elsevier, 2017), pp. 183-242.
- W. S. Yeap et al., Boron-doped diamond functionalization by an electrografting/alkyne-azide click chemistry sequence. ChemElectroChem 1, 1145-1154 (2014).
- C. Agnès et al., XPS study of ruthenium tris-bipyridine electrografted from diazonium salt derivative on microcrystalline boron doped diamond. Phys. Chem. Chem. Phys. 11, 11647 (2009).
- T. Strother et al., Photochemical functionalization of diamond films. Langmuir 18, 968-971 (2002).
- G.-J. Zhang et al., DNA micropatterning on polycrystalline diamond via one-step direct amination. 18 Langmuir 22, 3728-3734 (2006).
- R. Boukherroub et al., Photochemical oxidation of hydrogenated boron-doped diamond surfaces. Electrochem. Commun. 7, 937-940 (2005).
- C. E. Nebel, Electronic properties of CVD diamond. Semicond. Sci. Technol. 18, S1-S11 (2003).
- B. M. Nichols, J. E. Butler, J. N. Russell, R. J. Hamers, Photochemical functionalization of hydrogen-terminated diamond surfaces: A structural and mechanistic study. J. Phys. Chem. B 109, 20938-20947 (2005).
- X. Wang, P. E. Colavita, J. A. Streifer, J. E. Butler, R. J. Hamers, Photochemical grafting of alkenes onto carbon surfaces: Identifying the roles of electrons and holes. J. Phys. Chem. C 114, 4067-4074
- R. J. Hamers et al., Molecular and biomolecular monolayers on diamond as an interface to biology. Diam. Relat. Mater. 14, 661-668 (2005).
- N. Holmberg-Douglas, D. A. Nicewicz, Photoredox-catalyzed C-H functionalization reactions. Chem. Rev. 122, 1925-2016 (2022).
- L. Capaldo, D. Ravelli, M. Fagnoni, Direct photocatalyzed hydrogen atom transfer (HAT) for aliphatic C-H bonds elaboration. *Chem. Rev.* **122**, 1875–1924 (2022).
- J. Stöhr, NEXAFS Spectroscopy (Springer, Berlin Heidelberg, 1992).

- 27. B. F. Bachman et al., High-density covalent grafting of spin-active molecular moieties to diamond surfaces. Langmuir 37, 9222-9231 (2021).
- R. Szpera, D. F. J. Moseley, L. B. Smith, A. J. Sterling, V. Gouverneur, The fluorination of C—H bonds: Developments and perspectives. *Angew. Chem. Int. Ed.* **58**, 14824–14848 (2019).
- B. Lantaño, A. Postigo, Radical fluorination reactions by thermal and photoinduced methods. Org. Biomol. Chem. 15, 9954-9973 (2017).
- D. Lichtman, J. H. Craig, V. Sailer, M. Drinkwine, AES and XPS spectra of sulfur in sulfur compounds. Appl. Surf. Sci. 7, 325-331 (1981).
- R. K. Quinn et al., Site-selective aliphatic C-H chlorination using N -chloroamides enables a synthesis of chlorolissoclimide. J. Am. Chem. Soc. 138, 696-702 (2016).
- W. L. Czaplyski, C. G. Na, E. J. Alexanian, C.-H. Xanthylation, A synthetic platform for alkane functionalization. J. Am. Chem. Soc. 138, 13854-13857 (2016).
- C. A. G. N. Montalbetti, V. Falque, Amide bond formation and peptide coupling. Tetrahedron 61, 10827-10852 (2005).
- K. G. Latham, W. M. Dose, J. A. Allen, S. W. Donne, Nitrogen doped heat treated and activated hydrothermal carbon: NEXAFS examination of the carbon surface at different temperatures. Carbon 128, 179-190 (2018).
- Y. Zubavichus, A. Shaporenko, M. Grunze, M. Zharnikov, Innershell absorption spectroscopy of amino acids at all relevant absorption edges. *J. Phys. Chem. A* 109, 6998–7000 (2005).
 V. S. Smentkowski, J. T. Yates, Fluorination of diamond surfaces by irradiation of perfluorinated alkyl
- iodides. Science 271, 193-195 (1996).
- H.-B. Yang, A. Feceu, D. B. C. Martin, Catalyst-controlled C-H functionalization of adamantanes using selective H-atom transfer. *ACS Catal.* **9**, 5708–5715 (2019).
- D. Ravelli, M. Fagnoni, T. Fukuyama, T. Nishikawa, I. Ryu, Site-selective C-H Functionalization by decatungstate anion photocatalysis: Synergistic control by polar and steric effects expands the reaction scope. ACS Catal. 8, 701-713 (2018).
- F. J. Aguilar Troyano, K. Merkens, A. Gómez-Suárez, Selectfluor® radical dication (TEDA 2+.) A versatile species in modern synthetic organic chemistry. Asian J. Org. Chem. 9, 992-1007 (2020).
- F. G. Bordwell, J. A. Harrelson Jr., T. Y. Lynch, Homolytic bond dissociation energies for the cleavage of. alpha.-nitrogen-hydrogen bonds in carboxamides, sulfonamides, and their derivatives. The question of synergism in nitrogen-centered radicals. J. Org. Chem. 55, 3337-3341 (1990).
- E. C. Gentry, R. R. Knowles, Synthetic applications of proton-coupled electron transfer. Acc. Chem. Res. 49, 1546-1556 (2016).
- 42. D. S. Timofeeva, A. R. Ofial, H. Mayr, Kinetics of electrophilic fluorinations of enamines and carbanions: Comparison of the fluorinating power of N-F reagents. J. Am. Chem. Soc. 140, 11474-11486 (2018).
- D. D. M. Wayner, D. J. McPhee, D. Griller, Oxidation and reduction potentials of transient free radicals. J. Am. Chem. Soc. 110, 132-137 (1988).
- W. K. Weigel, H. T. Dang, A. Feceu, D. B. C. Martin, Direct radical functionalization methods to access substituted adamantanes and diamondoids. Org. Biomol. Chem. 20, 10-36 (2022).
- M. B. A. Olia, P. S. Donnelly, L. C. L. Hollenberg, P. Mulvaney, D. A. Simpson, Advances in the surface functionalization of nanodiamonds for biological applications: A review. ACS Appl. Nano Mater. 4, 9985-10005 (2021).
- Y. L. Zhong, K. P. Loh, The chemistry of C-H bond activation on diamond. Chem. Asian J. 5, 1532-1540 (2010).
- H. A. Girard et al., Surface properties of hydrogenated nanodiamonds: A chemical investigation. Phys. Chem. Chem. Phys. 13, 11517 (2011).
- Z. Yuan et al., Charge state dynamics and optically detected electron spin resonance contrast of shallow nitrogen-vacancy centers in diamond. Phys. Rev. Res. 2, 033263 (2020).
 A. Stacey et al., Depletion of nitrogen-vacancy color centers in diamond via hydrogen passivation.
- Appl. Phys. Lett. 100, 071902 (2012).
- L. M. Pham et al., NMR technique for determining the depth of shallow nitrogen-vacancy centers in diamond. Phys. Rev. B 93, 045425 (2016).

- 51. G. De Lange, Z. H. Wang, D. Ristè, V. V. Dobrovitski, R. Hanson, Universal dynamical decoupling of a single solid-state spin from a spin bath. Science 330, 60-63 (2010).
- M. Kaviani et al., Proper surface termination for luminescent near-surface NV centers in diamond. Nano Lett. 14, 4772-4777 (2014).
- N. Aslam et al., Nanoscale nuclear magnetic resonance with chemical resolution. Science 357, 67-71
- A. Laraoui et al., High-resolution correlation spectroscopy of 13C spins near a nitrogen-vacancy
- centre in diamond. *Nat. Commun.* **4**, 1651 (2013).
 P. Harder, M. Grunze, R. Dahint, G. M. Whitesides, P. E. Laibinis, Molecular conformation in Oligo(ethylene glycol)-terminated self-assembled monolayers on gold and silver surfaces determines their ability to resist protein adsorption. *J. Phys. Chem. B* **102**, 426–436 (1998). J. Rovny *et al.*, Nanoscale covariance magnetometry with diamond quantum sensors. *Science* **378**,
- 56 1301–1305 (2022).
- J. M. Boss, K. S. Cujia, J. Zopes, C. L. Degen, Quantum sensing with arbitrary frequency resolution. Science 356, 837-840 (2017).

- 58. M. Orrit, T. Ha, V. Sandoghdar, Single-molecule optical spectroscopy. Chem. Soc. Rev. 43, 973 (2014).
- 59. V. Seshan et al., Hydrogen termination of CVD diamond films by high-temperature annealing at atmospheric pressure. J. Chem. Phys. 138, 234707 (2013).
- Z.-H. Zhang et al., Neutral silicon vacancy centers in undoped diamond via surface control. Phys. Rev. Lett. 130, 166902 (2023).
- 61. B. L. Dwyer et al., Probing spin dynamics on diamond surfaces using a single quantum sensor. PRX Quantum 3, 040328 (2022).
- D. B. Bucher et al., Quantum diamond spectrometer for nanoscale NMR and ESR spectroscopy. Nat. Protoc. 14, 2707-2747 (2019).
- S. T. Nguyen, "Proton-Coupled Electron Transfer in Organic Synthesis and Materials Science: Photochemical Strategies for Olefin Hydroamidation, Biomass Valorization, Plastic Recycling, and Diamond Surface Functionalization," PhD thesis, Princeton University, Princeton, NJ (2022).
- 64. L. V. H. Rodgers, "Engineering Highly Coherent Qubits by Correlating Surface Spectroscopy with Quantum Measurement," PhD thesis, Princeton University, Princeton, NJ (2023).